



3D POROUS MATERIALS

Programming 3D curved mesosurfaces using microlattice designs

Xu Cheng^{1,2†}, Zhichao Fan^{1,2,3†}, Shenglian Yao⁴, Tianqi Jin^{1,2}, Zengyao Lv^{1,2}, Yu Lan^{1,2}, Renheng Bo^{1,2}, Yitong Chen^{1,5}, Fan Zhang^{1,2}, Zhangming Shen^{1,2}, Huanhuan Wan³, Yonggang Huang^{6,7}, Yihui Zhang^{1,2*}

Cellular microstructures form naturally in many living organisms (e.g., flowers and leaves) to provide vital functions in synthesis, transport of nutrients, and regulation of growth. Although heterogeneous cellular microstructures are believed to play pivotal roles in their three-dimensional (3D) shape formation, programming 3D curved mesosurfaces with cellular designs remains elusive in man-made systems. We report a rational microlattice design that allows transformation of 2D films into programmable 3D curved mesosurfaces through mechanically guided assembly. Analytical modeling and a machine learning-based computational approach serve as the basis for shape programming and determine the heterogeneous 2D microlattice patterns required for target 3D curved surfaces. About 30 geometries are presented, including both regular and biological mesosurfaces. Demonstrations include a conformable cardiac electronic device, a stingray-like dual mode actuator, and a 3D electronic cell scaffold.

Three-dimensional (3D) cellular microstructures are ubiquitous in living organisms, where they play diverse, irreplaceable roles in 3D shape formation (7–4), synthesis and transport of nutrients (5, 6), and regulation of growth and reproduction (7, 8). For example, the nonuniformly distributed cellular microstructures in the *Physalis philadelphica* berry and the *Silene vulgaris* flower, which form closed cages, offer a sufficient stiffness to support their oval calyx sacs (Fig. 1A, left and middle left); the intricate, vascular networks in cabbage leaves can locally shrink and unilaterally thicken at reduced temperatures, leading to the formation of a multilayer spherical shape (Fig. 1A, middle right); and the honeycomb-like cellular microstructures with hexagonal chambers throughout the cell wall of the *Stephanopyxis turris* diatom enhance the efficiency of its photosynthesis (Fig. 1A, right) (7). Because of the high surface areas, large pore volumes, and excellent mechanical and thermal properties of cellular structures, cellular designs have been exploited in the development of materials and functional systems (9, 10). Examples include lattice materials and foams with high specific stiffness, specific strength, and impact resistance (3, 11–15); porous elec-

trodes with small ion diffusion distances and large percentages of active materials for high-power lithium ion batteries (16, 17); artificial tissues and organs with hierarchical vascularized networks capable of oxygen and nutrient supply and waste removal (5, 6, 18); electromagnetic metamaterials capable of blocking, absorbing, enhancing, or bending electromagnetic waves (19); and metal-organic frameworks for water-splitting and oxygen-reduction reactions (20).

Inspired by cellular biological surfaces such as those shown in Fig. 1A, we developed a microlattice design strategy as a powerful route to achieve the desired stiffness distribution of 2D microfilms, thereby allowing their transformation into programmable 3D curved mesosurfaces using mechanically guided assembly. We established both an analytical model and a machine learning-based computational approach for the inverse design of target 3D curved mesosurfaces from 2D microlattice patterns with optimized distributions of porosity and cell sizes. Although inverse design methods of 2D-to-3D assembly have been reported for strategies relying on spatial stiffness control of thin films using thickness engineering (21, 22), soft active materials with programmable strain distributions (23–27), or constrained optimization of geometries and rotations of unit cells in kirigami and origami tessellations (28–31), the limitations of applicable materials and length scales have impeded their utility in 3D microelectronic devices (32, 33).

Microlattice design strategy for curvature programming of 3D mesosurfaces

Figure 1 illustrates the key concepts and capabilities of the bioinspired microlattice design strategy. This strategy introduces a 2D thin film with an engineered lattice pattern consisting of spatially varying triangular units and micrometer-

sized ribbons. The triangle lattice design is exploited instead of cellular designs with circular holes because of the relieved stress concentration and the excellent adaptability to complexly shaped edges (fig. S1). Figure 1B presents a schematic illustration of the microlattice design strategy using a circular design domain \mathfrak{R} as an example. We used triangular lattices to discretize the prescribed design domain (fig. S2), dividing the domain into N triangular units with M lattice nodes. L_{ik} (where $k = 1, 2, 3$) and φ_i are the side length and the porosity of the i^{th} triangular unit (where $i = 1, \dots, N$); $\varphi_i = 0$ and 1 denote two limit conditions, i.e., the solid material region without any porosity and the region without any material, respectively. Considering the stretching-dominated mechanism of the triangular lattice, the effective modulus (E_i) scales with the relative density ($\bar{\varphi}_i = 1 - \varphi_i$) of the unit, i.e., $E_i \propto (1 - \varphi_i)$, and therefore the distribution of microlattice porosity serves as a crucial parameter to adjust the stiffness distribution. We use Ω to denote the set of nodes (with M_{bond} nodes in total) that are bonded with a prestretched elastomer (prestrains, ε_X and ε_Y) in the mechanical assembly. Accordingly, the in-plane displacements \mathbf{D}_j ($\mathbf{D}_j = [d_{jX}, d_{jY}]$, $j = 1, 2, \dots, M_{\text{bond}}$) are applied to this node set Ω to trigger the 2D-to-3D assembly, where d_{jX} and d_{jY} are the displacement components of the j^{th} node along X and Y directions. Once the porosity distribution φ_i , the node set Ω of bonding sites, and the prestrain (ε_X and ε_Y) are given, the 3D mesosurface resulting from the mechanical assembly can be determined, corresponding to a forward problem. Figure S3 provides a set of examples with the same square-shaped design domain \mathfrak{R} , bonding sites, and uniaxial prestrain (30%). Assigning different porosity (φ_i) distribution results in distinct 3D surface geometries, indicating a crucial role of porosity distribution in tailoring the assembled mesosurface geometry.

The practical utility of the microlattice strategy requires a rational inverse design method as the theoretical basis. Herein, the inverse design problem focuses on determining the porosity distribution, bonding sites, and prestrain for a target 3D surface and a prescribed number (N) of triangular units. An octopus-like mesosurface serves an example to illustrate the key procedure of the inverse design (Fig. 1C). The design target (fig. S4A) is derived by simplifying the complex biological surface, which consists of an axisymmetric “head” region and eight curvy “tentacles.” Discretizing the head region into eight pieces of subsurfaces interconnected in the central region allows utility of a beam theory-based model (see the supplementary text for details) to obtain distributions of bending stiffness and porosity in the 2D precursor. The various tentacle shapes can be also reproduced using

¹Applied Mechanics Laboratory, Department of Engineering Mechanics, Tsinghua University, Beijing 100084, P.R. China.

²Laboratory of Flexible Electronics Technology, Tsinghua University, Beijing 100084, P.R. China. ³College of Mechanical and Vehicle Engineering, Hunan University, Changsha 410082, P.R. China.

⁴School of Materials Science and Engineering, University of Science and Technology Beijing, Beijing 100083, P.R. China. ⁵Department of Automation, Tsinghua University, Beijing 100084, P.R. China. ⁶Querry Simpson Institute for Bioelectronics, Northwestern University, Evanston, IL 60208, USA.

⁷Departments of Civil & Environmental Engineering, Mechanical Engineering, and Materials Science & Engineering, Northwestern University, Evanston, IL 60208, USA.

*Corresponding author. Email: yihuizhang@tsinghua.edu.cn

†These authors contributed equally to this work.

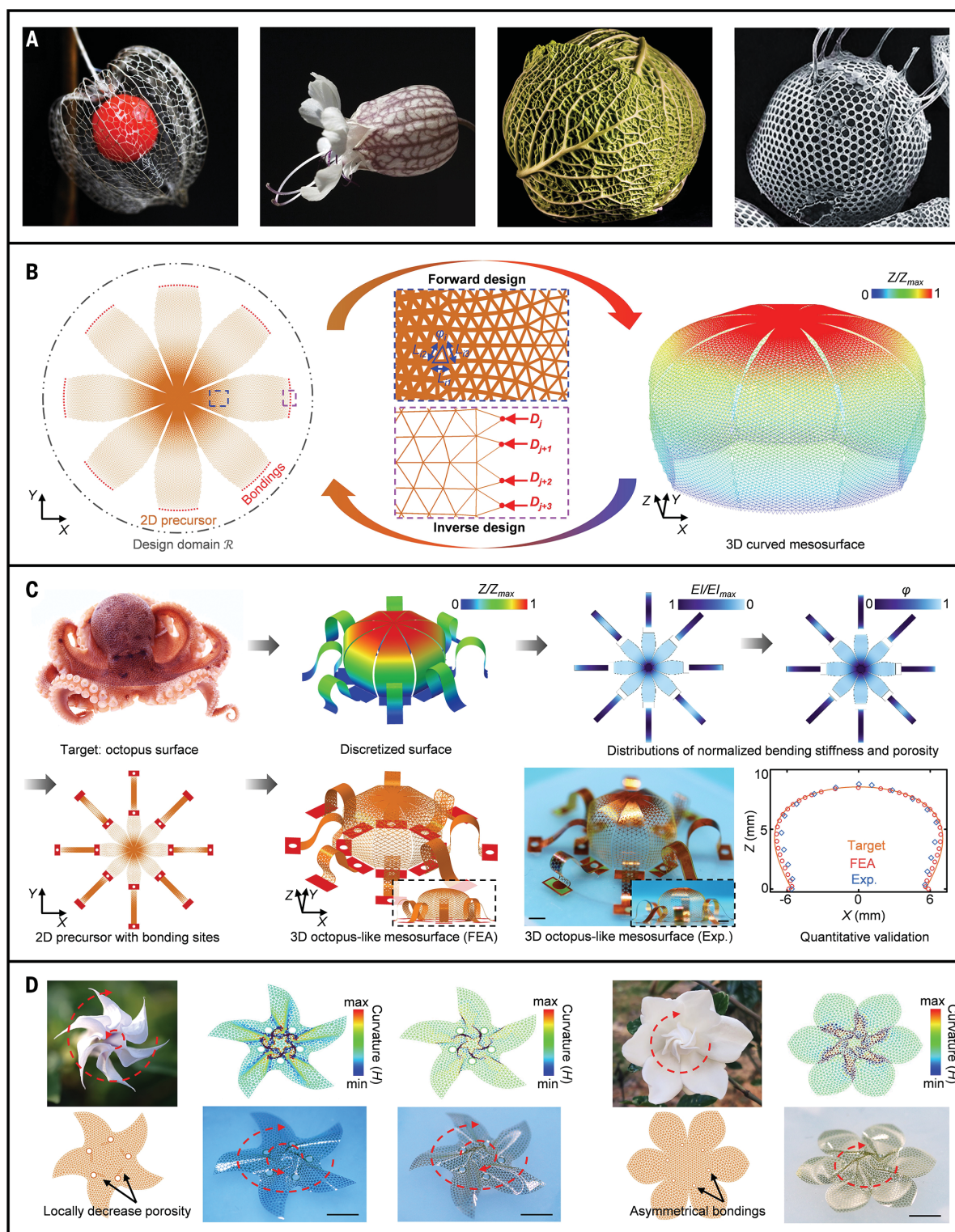


Fig. 1. Conceptual illustrations of curvature programming of 3D mesosurfaces by bioinspired microlattice design strategy. (A) Optical images of a *Physalis philadelphica* berry (left) and *S. vulgaris* flower (middle left) with oval, reticular calyx sacs; multilayer spherical cabbage leaves with intricate, vascular networks (middle right); and an *S. turris* diatom with a honeycomb-like cellular cell wall [reproduced with permission from Jantschke et al. (1), copyright 2014, The Royal Society of Chemistry]. (B) Schematic illustrations of forward and inverse designs of 3D curved mesosurfaces in the framework of the bioinspired

microlattice design strategy. Here, φ_i and L_{ik} (where $k = 1, 2, 3$) represent the porosity and side lengths of triangular unit cell numbered i in the design domain \mathfrak{R} , respectively, and \mathbf{D}_j is the displacement vector (d_{jX}, d_{jY}) of the node numbered j in the bonding regions. (C) FEA and experimental results of the inverse design of an octopus-like mesosurface with an optimized microlattice pattern based on a discretized approach. (D) Two flower mesostructures (left: *D. stramonium*, right: *G. jasminoides* Ellis) and bioinspired designs with bonding sites distributed inside the 2D microlattice. Scale bars, 2 mm.

this model. Then, the 2D microlattice pattern can be generated, along with the node set of bonding sites. The assembled 3D surface geometry based on finite element analysis (FEA) and experimental measurements are both in excellent agreement with the design target (Fig. 1C and fig. S4, B and C). The maximum principal strain is <1% in most regions of the octopus-like mesosurface, indicating that the fracture failure would not occur in commonly used electronic materials (e.g., Si, Au, Cu, and Ti) during assembly (fig. S4B). Here, the micro-fabrication technologies (materials and methods and figs. S5 to S9) allowed fabrication of patterned 2D microlattice in a bilayer of 200 nm Cu and 12 μm polyimide (PI), with a minimum ribbon width of 10 μm . The experiments of mechanically guided assembly followed procedures similar to those reported previously (fig. S10) (34, 35).

The microlattice design strategy confers a locally discrete yet globally continuous geometric feature of the microfilm, which enables a discreteness-mediated deformation mechanism inaccessible to solid microfilms. Such a discreteness-mediated deformation mechanism mainly occurs in microfilms with inner bonding sites, where localized deformations usually develop. A circular-shaped microfilm serves as an example to describe this mechanism, in which four symmetrically distributed inner bonding sites are assigned (fig. S11). Although the structural geometry and loading conditions are symmetric with regard to the X and Y axes, the buckling deformations display two possible modes that are mediated by the discreteness. For solid or densely distributed microlattice films, a chiral mode involving twisting deformations is more energetically favorable (fig. S11, B and C). When the microlattice is sufficiently sparse to accommodate bending-dominated deformations of ribbon components, the symmetric mode becomes more energetically favorable. Although the solid microfilm shows a chiral buckling mode, the twisting orientation is random and not controllable. Harnessing the discreteness-mediated deformation of microlattice films offers an avenue to 3D mesosurfaces with controlled chirality, e.g., by introducing slightly reduced porosity at the intermediate region of two bonding sites (fig. S12). Figure 1D and fig. S13 present two mesosurfaces inspired by *Datura stramonium* and *Gardenia jasminoides* Ellis, in which the chirality is tailored by the porosity-governed method (see the supplementary text).

Microlattice design methods for the rational assembly of 3D mesosurfaces

A beam theory-based model allows the inverse design of 2D ribbon mesostructures and axis-symmetric mesosurfaces (Fig. 2 and figs. S14 to S20). By homogenizing a straight, ribbon-shaped microlattice as a solid ribbon structure

and using the Euler-Bernoulli beam theory, the key design parameters [including the porosity $\varphi(S)$ and the prestrain ε_{pre}] for a target ribbon can be obtained analytically (see the supplementary text and figs. S14 to S16). Most axis-symmetric 3D surfaces are nondevelopable and therefore cannot be assembled directly from geometrically continuous 2D films without involving large membrane strains (e.g., >5%), which are not tolerable for most inorganic electronic materials. We introduce a discretization-based approximation method to allow utility of the beam theory-based model in the inverse design of axis-symmetric mesosurfaces. The method divides the target surface uniformly into n subsurfaces (fig. S17), each of which can be considered as a ribbon with a nonuniform width. Then, the porosity distribution $\varphi(S)$ and the prestrain ε_{pre} can be determined for the target subsurface. Figure 2A presents a hemispherical mesosurface approximated with 10 subsurfaces (supplementary text), where optical images and numerical simulations of the assembled 3D mesosurface are in close accordance with the target surface. The experiments used a bilayer of 200 nm Si and 8 μm PI in the fabrication, and the resulting hemispherical mesosurface has a diameter of ~2 mm (movie S1). Similarly, the proposed method allows for the inverse design of spherical caps (100 nm Au or Ti and 8 μm PI) (fig. S18, A to C) and hemi-ellipsoidal mesosurfaces (100 nm Au or Ti and 12 μm PI) with various aspect ratios (3, 2/3, and 1/3) (fig. S18, D to F). Fairly close 3D mesosurfaces can be obtained through use of only 10 subsurfaces in the discretization (Fig. 2A and fig. S18, A to F). These results illustrate the effectiveness of the inverse design method based on the microlattice strategy.

Introducing inner bonding sites allows the curvature of the assembled 3D mesosurface to vary its sign, thereby expanding the range of 3D mesosurfaces. Figure 2B presents a volcano-like mesosurface (100 nm Ti and 8 μm PI) with a crateriform concavity (~1.4 mm in diameter) at the central region. Assigning a high level of porosity (90%) to the joint region of inner and outer surfaces enables programmable folding deformations to reproduce the geometric feature of the slope discontinuity (movie S2). With use of a single inner bonding site, donut-like 3D mesosurfaces can also be accurately attained (fig. S18, G and H). Adding more inner bonding sites allows combination of two or more customized 3D mesosurfaces, enriching the accessible range of axis-symmetric mesosurfaces. Figure 2C, fig. S18I, and movie S3 provide two palace-like mesostructures composed of a torus at the outer region and a cylinder (or a hemisphere) at the inner region. Approximately closed-form geometries are also possible, with two examples shown in Fig. 2, D and E, and fig. S19, D and E.

The above beam theory-based model also allows for the inverse design of 3D mesosurfaces with rotational symmetries, including complex biomimetic mesosurfaces reconstructed from real plants. For example, the blueberry flower has five petals and a style, and their shapes can be reconstructed through discrete-point sampling to serve as our design target (Fig. 2F, left, and fig. S20A). Then, the bilayer 2D precursor patterns and the prestrain can be determined through the inverse design method (Fig. 2F, middle left, and fig. S20B). The resulting biomimetic microlattice structure is shown in the middle of Fig. 2F. Similarly, a biomimetic *P. philadelphica* berry surrounded with a closed oval calyx sac can be inversely designed and fabricated (Fig. 2G and fig. S20, C and D). This inverse design method can be further extended to curvy mesosurfaces with a slight degree of asymmetry. In this case, the mesosurface is discretized into a certain number of uneven curvy ribbons, and each ribbon component can be reproduced by optimizing the porosity distribution and prestrain. Two examples are provided in Fig. 2, H and I, and fig. S21, where the design targets mimic a garden spider's abdomen and an asymmetric flowerpot.

Design of a strain-limiting frame to connect bonding sites of as-assembled 3D mesosurfaces allows their isolation from the bulky elastomeric substrate without altering their geometric configurations (fig. S22). On the basis of this facile isolation method, freestanding 3D mesosurfaces with diverse configurations are fabricated, including an octopus head-like mesosurface, a hemi-ellipsoidal mesosurface, and spherical caps, with the lateral size spanning from ~600 μm to ~14 mm (Fig. 2J and fig. S23). Mechanics modeling suggested that the stiffness ratio between the 3D mesostructure and the strain-limiting frame is the dominant parameter that affects the shape fixation (see the supplementary text and fig. S24). In addition, the extended material compatibility, broad applicable length scales, and rich structural topology (Fig. 2, J and K, and figs. S25 to S27) suggest versatile capabilities of the microlattice strategy for designing 3D functional devices and Microsystems.

If the target 3D surface cannot be discretized into a group of symmetric ribbons, then the above beam theory-based model considering only bending deformations will not work. Introducing a machine learning algorithm allows for the establishment of a powerful inverse design method for 3D mesosurfaces with both symmetric and asymmetric configurations. Using the seashell surface as an example (Fig. 3A), the method starts with discretizing the 3D curved surface into a set of 3D feature points ($X_i, Y_i, Z_i, i = 1 \dots N_p$, where N_p is the total point number) using strategic cuts that can capture key geometric features (i.e., radial

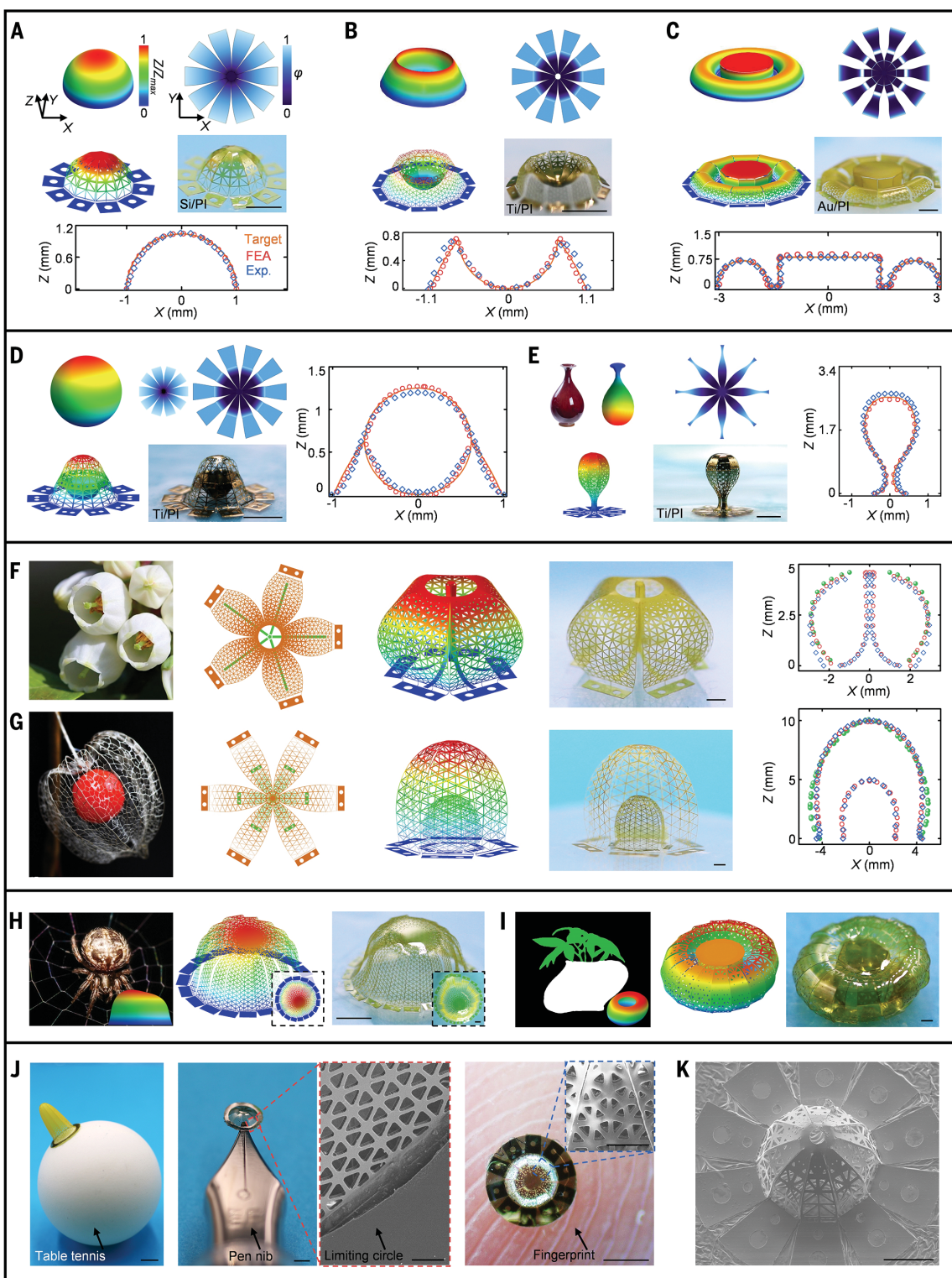


Fig. 2. Inverse designs of 3D curved mesosurfaces based on an analytical model. (A to C) Target geometry, porosity distribution of the 2D precursor pattern, and corresponding FEA and experimental results for a hemispherical mesosurface (A), a volcano-like mesosurface (B), and a palace-like mesosurface (C). (D and E) Inverse design of closed-form 3D mesosurfaces: a suspended spherical mesosurface (D) and a vase-like mesosurface (E). (F and G) Inverse design of two plant mesosurfaces with bilayer layouts: blueberry flower (F) and *P. philadelphica* berry (G). Green dots are sampled from the plant surfaces.

(H) Target geometry, FEA, and experimental results of an asymmetric surface that resembles the curved abdomen of a garden spider. (I) Similar results for the inverse design of an asymmetric flowerpot. (J) 3D isolated mesosurfaces with different aspect ratios and length scales (from millimeter to micrometer). Scale bars, 5 mm, 1 mm, and 500 μ m in the three optical images from left to right, respectively, and 100 μ m in the SEM images. (K) SEM image of a hemispherical microsurface (30 nm Ti and 2.7 μ m PI). Scale bars: (A) to (I), 1 mm; (K), 100 μ m.

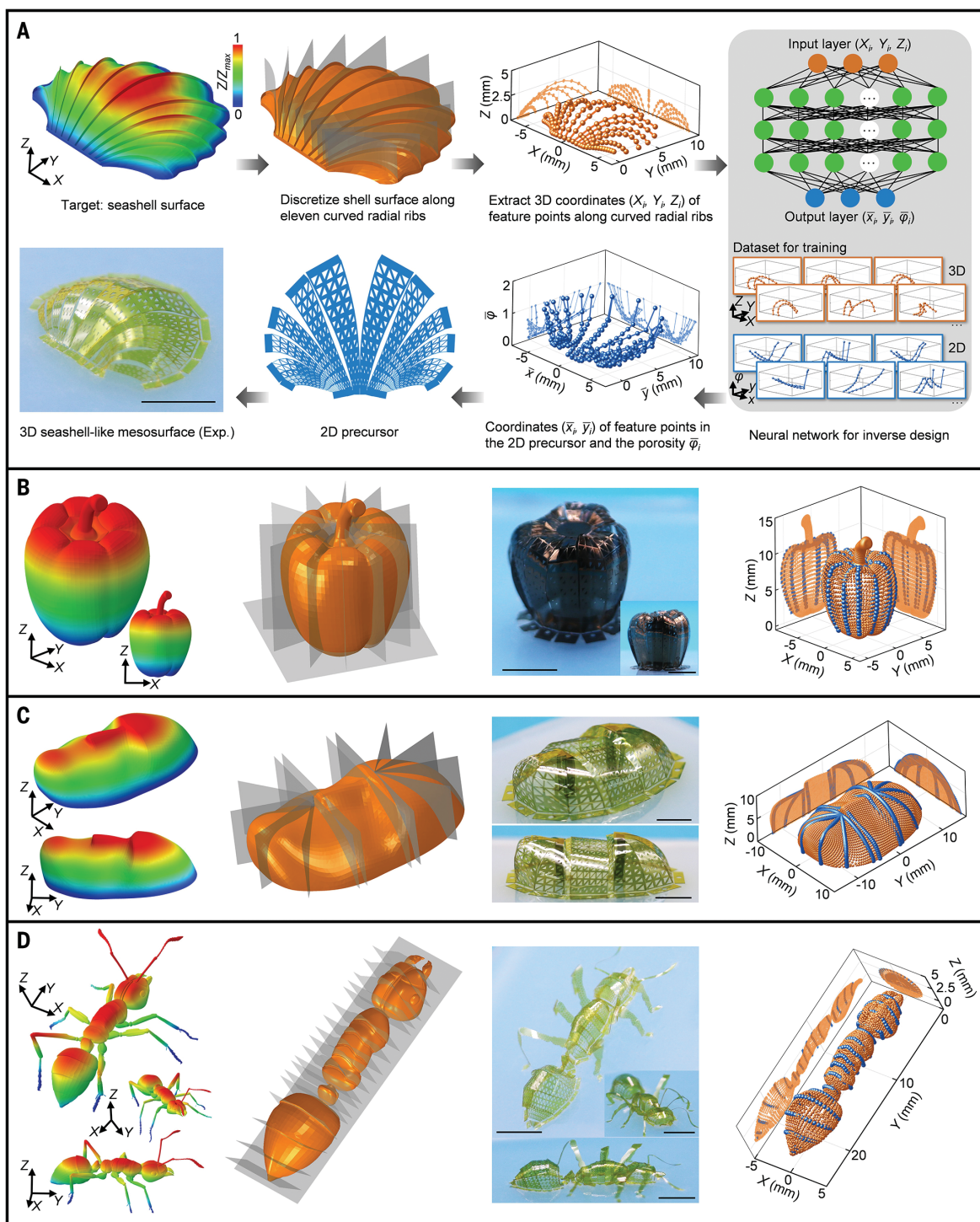


Fig. 3. Inverse designs of 3D complex mesosurfaces using a point cloud-based machine learning method. (A) Schematic illustrations of the process of the inverse design for a seashell mesosurface (20 nm Ti and 7 μm PI). (B) Target geometries, discretization strategies, experimental results, and comparisons between the computed point cloud (blue) and the design target (orange) for a pimento-like

mesosurface (200 nm Ti and 7 μm PI), which is divided into discretized ribbon components using a set of planes across a central line. (C) Similar results for a mask-like mesosurface (20 nm Ti and 7 μm PI) with regional discretization through radial and parallel cuts. (D) Similar results for an ant-like surface (20 nm Ti and 7 μm PI) based on a cutting strategy similar to CT scanning. Scale bars, 5 mm.

ribs in this example). A point cloud-based artificial neural network (36) is exploited to predict the 2D point coordinates (\bar{x}_i, \bar{y}_i) and their corresponding porosity ($\bar{\varphi}_i$) on the basis of the training by generating a dataset through FEA

(see the supplementary text and figs. S28 to S32). Then, the 2D microlattice pattern containing 12 separate ribbons and bonding sites can be generated, given the optimal set of ($\bar{x}_i, \bar{y}_i, \bar{\varphi}_i$) and prescribed meshing method. The

loadings [i.e., displacements (Δ_x, Δ_y) and rotation angle (Θ) of bonding sites in the $X-Y$ plane] applied to the 2D ribbon precursors can be determined directly by the coordinates of bonding edges in the 2D precursor and

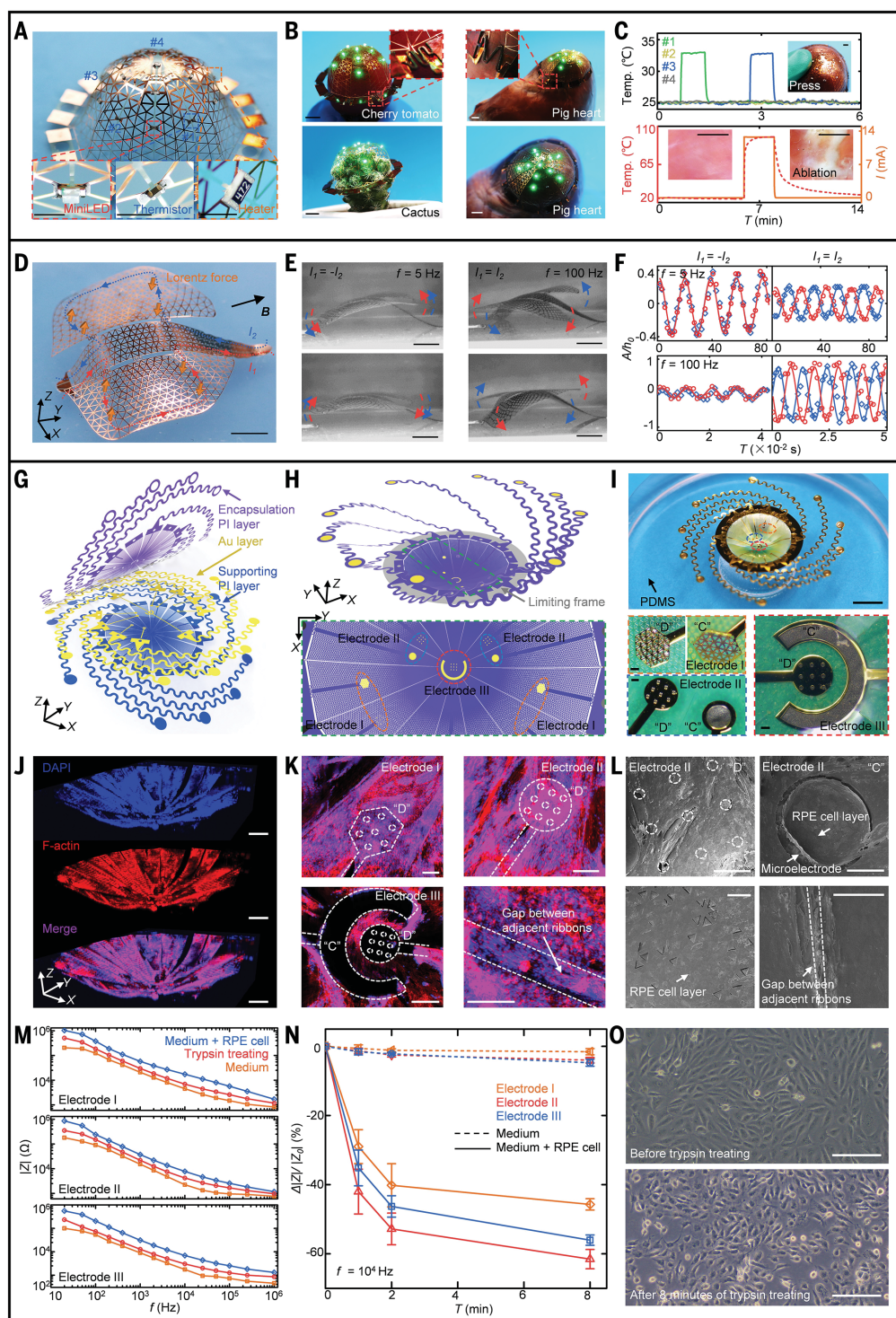
target seashell surface. Considering the negligible axial elongation or compression of ribbon components during buckling deformations, each ribbon component typically requires a distinct loading condition, indicating that the entire seashell surface cannot be formed through a single-step assembly on the same substrate. Each ribbon component is assembled on a separate substrate (see the supple-

mentary text) and then transferred onto the same platform using the aforementioned strain-limiting frame to form the entire 3D mesosurface (figs. S33 and S34). Quantitative comparisons of feature-point coordinates in target seashell surface, FEA, and experiments show a high degree of agreement (fig. S35). Refining the discretization with more strategic cuts leads to an enhanced agreement of the

resulting mesosurface and the design target (fig. S36).

As illustrated above, the mapping between 3D complex mesosurfaces and 2D microlattice films is actually simplified into the one between a set of 3D point cloud (X_i, Y_i, Z_i) and another ($\bar{x}_i, \bar{y}_i, \bar{\varphi}_i$). Therefore, the computational cost could be reduced considerably to facilitate the inverse design of complex 3D

Fig. 4. Applications of 3D curved meso-surfaces based on bioinspired micro-lattice designs. (A) Optical image of a breathable, hemispherical electronic device that integrates mini-LEDs, chip thermistors, and a heater. (B) Conformal electronic device wrapped around the cherry tomato, cactus, and apical region of a pig heart. (C) Measured temperature change of the heart surface (top) under a finger press and during the thermal ablation therapy in a local region of the heart (bottom). Scale bars: (A) and (C), 1 mm; (B), 5 mm. (D) Optical image of a stingray-like actuator with two circuits arranged on two sides of the body. (E and F) Optical images and amplitude responses of two vibration modes (left: top-down mode; right: left-right mode) of the 3D actuator excited by Lorentz forces. A and h_0 are the vibrational amplitude and initial height of front tips of two “fins,” respectively. Scale bars, 5 mm. (G to I) Schematic illustrations of the 2D precursor designs (G), FEA results of assembled 3D configurations (H), and corresponding experimental results (I) of an electronic cell scaffold. Scale bars in (I), 5 mm (top) and 100 μ m (bottom). (J and K) Fluorescence-stained images and magnified images of the electronic cell scaffold with RPE cells. Scale bars: (J), 1 mm; (K), 200 μ m. (L) SEM images of local regions after freeze-drying. Scale bars, 100 μ m. (M) Impedance curves for electrodes I, II, and III with three different conditions. (N) Relative changes of the impedance at 10 kHz as a function of the trypsin treating time for three different electrodes. The average values of four independent experiments are shown with SD values. (O) Optical images of the RPE cells before and after 8 min of trypsin treating. Scale bars, 20 μ m.



surfaces. The strategy used to discretize the target surface is important in this method. For 3D surfaces with an approximate rotational symmetry, a set of planes that cross a central line can divide the mesosurface into discretized ribbon components. The pimento and carambola serve as two mesosurfaces that can be inversely designed following this discretization strategy (Fig. 3B and figs. S37 and S38, A and B). Extraction of spatial coordinates of feature points allows a quantitative shape comparison between biomimetic microlattice structures and target surfaces (Fig. 3B and figs. S37, right, and S39, A and B). For mesosurfaces without a clear symmetry, the target surface can be first divided into certain subsurface parts according to the geometric feature, and then each part can be further discretized using an appropriate strategy (e.g., radial or parallel cuts). As an example, Fig. 3C and figs. S38C and S39C present results of an inverse design for a target surface that resembles a face mask. Here, the inverse design begins with cutting the surface into three parts, followed by discretizing these parts into five, three, and five ribbon components, for the “forehead,” “nose,” and “chin” parts, respectively. Figure 3D illustrates the use of the proposed inverse design method in generating an ant-like mesostructure in which the main body part is discretized using a cutting strategy similar to computed tomography (CT) scanning. The six legs and two tentacles are designed separately and then added to the main body part after its assembly. The entire ant-like microlattice structure consisting of 4034 microtriangles and 7826 microribbons accurately reproduces the design target (Fig. 3D and figs. S38D and S39D), showing the capability of the point cloud-based method in designing highly complex 3D mesosurfaces.

Device applications based on bioinspired microlattice designs

The bioinspired microlattice designs allow the construction of 3D electronic systems with the desired curvature distributions for either conforming to or replicating the curvy surfaces of biological tissues and organs. Figure 4A presents a breathable, hemispherical electronic device for cardiac sensing, optical stimulation, and thermal ablation. This device consists of 11 blue mini-LEDs, four chip thermistors, and one heater, and copper wires (250 nm) sitting on PI microlattice frames (10 μm) serve as the electrical connection (fig. S40). Here, we introduce optimized serpentine structures as strain-limiting frames in which the as-assembled hemispherical shape can not only be well maintained in the freestanding state, but can also be deformable to adapt to nonspherical surfaces to yield high signal-to-noise ratio temperature sensing (Fig. 4B and Fig. 4C, top; fig. S41; and movie S4). The microlattice design

not only reduces physical constraints [e.g., interfacial adhesion and wrinkles (37, 38); fig. S41F] on the heart, but also provides microchannels for the lubricating fluid in the pericardium to avoid pericardiosympathy. This device could be used for the treatment of heart arrhythmias (39). An array of blue micro-LEDs could perform optogenetic therapy with large area of optical stimulation, and the microheater is capable of localized thermal ablation to suppress abnormal electrical signals on the heart surface (Fig. 4C, bottom).

Biomimetic 3D mesostructures that imitate the dynamic characteristics of living organisms are also possible using the microlattice designs. Figure 4D, fig. S42, and movie S5 show a stingray-like 3D mesostructure with a curved body and a pair of “fan-shaped fins.” Two circuits integrated with the fins can generate periodically varying Lorentz forces to the 3D mesostructure under a fixed magnetic field (**B**) along the body length direction (Fig. 4D and fig. S42). Different vibration modes can be excited by varying current directions in the two circuits and adjusting their frequency (Fig. 4, E and F). The difference between measured resonant frequencies (5 and 100 Hz) of these two modes is evident, because of their distinct deformation features.

Development of 3D biological models and platforms that mimic *in vivo* 3D microenvironments has important implications for investigating fundamental behaviors (e.g., growth, apoptosis, and pathogenesis) of cells. For example, the retinal pigment epithelium (RPE) cells in the 3D curved surface of the outer blood-retinal barrier–vascular complex are essential in transporting biological molecules between the retina and blood, but existing culture models of RPE cells are limited to 2D planar geometries (40). A spherical cap-shaped electronic cell scaffold with integrated sensing capabilities is presented here (Fig. 4, G to I; supplementary text; and fig. S43), in which the curvature radius (~7.5 mm) is close to that of rabbit RPE. RPE cells were planted on the 3D scaffold, and then cultured for 15 days with the medium changed every 2 days. Figure 4, J and K, provides fluorescent staining images of RPE cells growing on the electronic scaffold. It can be seen that RPE cells are uniformly spread across the whole curved surface because of the relatively closed configuration and micrometer-sized lattices (5 to 62 μm in microribbon length, which is similar in size to the RPE cells) of the 3D scaffold. As evidence, Figs. 4K, bottom right, and 4L and fig. S44 show that RPE cells could cross the gaps between adjacent ribbon components of the curved mesosurface to connect with each other. Results of impedance measurements based on the 3D electronic scaffold are shown in Fig. 4, M and N. Because RPE cells behave as dielectric materials when immersed in culture media under electrical stimulation

(41, 42), a distinct increase of impedance can be observed after growth of RPE cells on the scaffold (Fig. 4M). To test the sensitivity of impedance measurements to physiological activities of RPE cells, a trypsin solution was used to treat these cells, and the time responses of impedance were recorded (Fig. 4N). As the time of trypsin treating increases, the impedance drops rapidly and eventually stabilizes because trypsin causes RPE cells to contract and partially detach from the scaffold, as evidenced by the optical images shown in Fig. 4O and fig. S45. These results suggest the 3D electronic cell scaffold as a noninvasive platform for studying real-time, spatial distributions of physiological activities (e.g., growth and apoptosis) of cells.

Conclusion

The bioinspired microlattice design strategy and inverse design methods presented herein allow for the rational assembly of 2D films into desired 3D mesosurfaces with diverse geometries, from regular surfaces (e.g., hemispherical, spherical, hemi-ellipsoidal, and hemi-toroidal surfaces) to highly complex surfaces (e.g., those resembling a volcano, flower, fruit, octopus, and ant). In principle, the microlattice designs are applicable to a broad set of materials, including but not limited to those demonstrated in this work (silicon, metals, chitosan, polyimide, SU8, and laser-induced graphene). Compared with previous strategies (21–24) for local stiffness control, the proposed microlattice design enables fundamental advances in realizable geometries, applicable materials, and length scales of the assembled 3D surfaces (see the supplementary text). Demonstrations in conformal 3D cardiac electronic devices, a bionic dual-mode actuator, and a 3D electronic cell scaffold suggest promising application opportunities in bioelectronics, microelectromechanical systems, and micro-robotics. Additionally, the microlattice strategy can be used to design optical devices such as optical metasurfaces with angle-dependent reflectance (fig. S46).

REFERENCES AND NOTES

- A. Jantschke, C. Fischer, R. Hensel, H. G. Braun, E. Brunner, *Nanoscale* **6**, 11637–11645 (2014).
- E. E. Kuchen *et al.*, *Science* **335**, 1092–1096 (2012).
- F. V. Senhora, E. D. Sanders, G. H. Paulino, *Adv. Mater.* **34**, e2109304 (2022).
- W. Li *et al.*, *Nat. Electron.* **4**, 134–142 (2021).
- B. Grigoryan *et al.*, *Science* **364**, 458–464 (2019).
- L. Neufeld *et al.*, *Sci. Adv.* **7**, eabi9119 (2021).
- K. J. I. Lee *et al.*, *PLOS Biol.* **17**, e3000427 (2019).
- D. A. Dickerson, *Adv. Biol.* e2200067 (2022).
- S. Li *et al.*, *Nature* **592**, 386–391 (2021).
- D. M. Sussman *et al.*, *Proc. Natl. Acad. Sci. U.S.A.* **112**, 7449–7453 (2015).
- J. R. Greer, V. S. Deshpande, *MRS Bull.* **44**, 750–757 (2019).
- S. J. Yeo, M. J. Oh, P. J. Yoo, *Adv. Mater.* **31**, e1803670 (2019).
- S. N. Khaderi *et al.*, *Extreme Mech. Lett.* **10**, 15–23 (2017).
- L. R. Meza, J. M. J. Schormans, J. J. C. Remmers, V. S. Deshpande, *J. Mech. Phys. Solids* **125**, 276–297 (2019).
- A. J. D. Shaikjee, H. Cui, M. O’Masta, X. R. Zheng, V. S. Deshpande, *Nat. Mater.* **21**, 297–304 (2022).
- W. Li, J. Liu, D. Zhao, *Nat. Rev. Mater.* **1**, 16023 (2016).

17. Z. Qu *et al.*, *Adv. Energy Mater.* **12**, 2200714 (2022).
18. G. J. Pahapale *et al.*, *Adv. Sci. (Weinh.)* **9**, e2104649 (2022).
19. D. Schurig *et al.*, *Science* **314**, 977–980 (2006).
20. H. Hu *et al.*, *Nat. Chem.* **13**, 358–366 (2021).
21. Z. Fan *et al.*, *Adv. Mater.* **32**, e1908424 (2020).
22. M. Liu, L. Domino, D. Vella, *Soft Matter* **16**, 7739–7750 (2020).
23. J. H. Pikul *et al.*, *Science* **358**, 210–214 (2017).
24. J. W. Boley *et al.*, *Proc. Natl. Acad. Sci. U.S.A.* **116**, 20856–20862 (2019).
25. H. Aharoni, Y. Xia, X. Zhang, R. D. Kamien, S. Yang, *Proc. Natl. Acad. Sci. U.S.A.* **115**, 7206–7211 (2018).
26. A. Nojoomi, J. Jeon, K. Yum, *Nat. Commun.* **12**, 603 (2021).
27. K. Liu, F. Hacker, C. Daraio, *Sci. Robot.* **6**, eabf5116 (2021).
28. G. P. T. Choi, L. H. Dudte, L. Mahadevan, *Nat. Mater.* **18**, 999–1004 (2019).
29. R. Guseinov, C. McMahan, J. Pérez, C. Daraio, B. Bickel, *Nat. Commun.* **11**, 237 (2020).
30. L. Jin, A. E. Forte, B. Deng, A. Rafsanjani, K. Bertoldi, *Adv. Mater.* **32**, e2001863 (2020).
31. C. Baek, A. G. Martin, S. Poincloux, T. Chen, P. M. Reis, *Phys. Rev. Lett.* **127**, 104301 (2021).
32. M. Kim *et al.*, *Nat. Electron.* **3**, 546–553 (2020).
33. C. Becker *et al.*, *Nat. Commun.* **13**, 2121 (2022).
34. S. Xu *et al.*, *Science* **347**, 154–159 (2015).
35. Y. Zhang *et al.*, *Nat. Rev. Mater.* **2**, 17019 (2017).
36. Y. Guo *et al.*, *IEEE Trans. Pattern Anal. Mach. Intell.* **43**, 4338–4364 (2021).
37. C. Zhang, Y. K. Hao, B. Li, X. Q. Feng, H. Gao, *Soft Matter* **14**, 1681–1688 (2018).
38. X. Lin *et al.*, *Nat. Biomed. Eng.* **3**, 632–643 (2019).
39. J. Park *et al.*, *Sci. Transl. Med.* **8**, 344ra86 (2016).
40. D. Kent *et al.*, *Exp. Eye Res.* **76**, 213–219 (2003).
41. A. G. Montaño-Figueredo *et al.*, *Biosens. Bioelectron.* **128**, 37–44 (2019).
42. A. Bussooa *et al.*, *Adv. Sci. (Weinh.)* **7**, 1902999 (2020).

ACKNOWLEDGMENTS

We thank J. A. Rogers from Northwestern University for inspiring discussions. **Funding:** This work was supported by the National Natural Science Foundation of China (grants 12050004 and 12225206 to Y.Z. and grant 31800813 to S.Y.); the Tencent Foundation (XPLOTER Prize to Y.Z.); and the Institute for Guo Qiang, Tsinghua University (grant 2021GQ01009 to Y.Z.).

Author contributions: Y.Z. designed and supervised the research. X.C., Z.F., and Y.Z. led the structural designs and mechanics modeling with assistance from T.J., Y.C., H.W., and Y.H. X.C. led the fabrication work with assistance from Y.L. and Z.S. S.Y. and

X.C. led the design and characterization of electronic cell scaffold with assistance from Z.F. X.C. and F.Z. led the design and characterization of dual-mode actuators. Z.L., X.C., and R.B. led the metasurface design and simulations. Y.Z. and X.C. wrote the manuscript and designed the figures. All authors commented on the manuscript. **Competing interests:** The authors declare no competing interests. **Data and materials availability:** All data are available in the main text or the supplementary materials. **License information:** Copyright © 2023 the authors; some rights reserved; exclusive licensee American Association for the Advancement of Science. No claim to original US government works. <https://www.science.org/about/science-licenses-journal-article-reuse>

SUPPLEMENTARY MATERIALS

science.org/doi/10.1126/science.adf3824

Materials and Methods

Supplementary Text

Figs. S1 to S46

References (43–50)

Movies S1 to S5

Submitted 18 October 2022; accepted 1 March 2023

10.1126/science.adf3824

Programming 3D curved mesosurfaces using microlattice designs

Xu Cheng, Zhichao Fan, Shenglian Yao, Tianqi Jin, Zengyao Lv, Yu Lan, Renheng Bo, Yitong Chen, Fan Zhang, Zhangming Shen, Huanhuan Wan, Yonggang Huang, and Yihui Zhang

Science, 379 (6638), .
DOI: 10.1126/science.adf3824

Rational inverse design of 3D shapes

Nature has a wide range of tools for making cellular microstructures, such as those found in flowers, leaves, and other biological tissues. Despite advances in printing techniques, patterning porous, curved surfaces can be challenging. Cheng *et al.* developed an inverse design method to achieve complex three-dimensional (3D) surfaces through a subset of 2D films that are bonded together. Analytic modeling and computations to inverse design the 2D patterns allow for control of the final porosity. A wide range of examples are provided, including changes in the sign of the curvature. These structures can be fabricated from silicon, metals, chitosan, and polymers. —MSL

View the article online

<https://www.science.org/doi/10.1126/science.adf3824>

Permissions

<https://www.science.org/help/reprints-and-permissions>